# Nanoparticle packing within block copolymer micelles prepared by the interfacial instability method

| | |
|---|---|
| Journal: | *Soft Matter* |
| Manuscript ID | SM-ART-03-2018-000425.R1 |
| Article Type: | Paper |
| Date Submitted by the Author: | 28-Mar-2018 |
| Complete List of Authors: | Nabar, Gauri; The Ohio State University, William G. Lowrie Department of Chemical and Biomolecular Engineering<br>Winter, Jessica; The Ohio State University, William G. Lowrie Department of Chemical and Biomolecular Engineering, Biomedical Engineering<br>Wyslouzil, Barbara; The Ohio State University, William G. Lowrie Department of Chemical and Biomolecular Engineering; The Ohio State University, Department of Chemistry |
| | |

**SCHOLAR**ONE™
Manuscripts

# Soft Matter

## ARTICLE

# Nanoparticle packing within block copolymer micelles prepared by the interfacial instability method

Gauri M. Nabar[a], Jessica O. Winter[a,b], and Barbara E. Wyslouzil[a,c*]

The interfacial instability method has emerged as a viable approach for encapsulating high concentrations of nanoparticles (NPs) within morphologically diverse micelles. In this method, transient interfacial instabilities at the surface of an emulsion droplet guide self-assembly of block co-polymers and NP encapsulants. Although used by many groups, there are no systematic investigations exploring the relationship between NP properties and micelle morphology. Here, the effect of quantum dot (QD) and superparamagnetic iron oxide NP (SPION) concentration on the shape, size, and surface deformation of initially spherical poly(styrene-b-ethylene oxide) (PS-b-PEO) micelles was examined. Multi-NP encapsulation and uniform dispersion within micelles was obtained even at low NP concentrations. Increasing NP concentration initially resulted in larger numbers of elongated micelles and cylinders with tightly-controlled diameters smaller than those of spherical micelles. Beyond a critical NP concentration, micelle formation was suppressed; the dominant morphology became densely-loaded NP structures that were coated with polymer and exhibited increased polydispersity. Transmission electron microscopy (TEM) and small angle X-ray scattering (SAXS) revealed that NPs in densely-loaded structures can be well-ordered, with packing volume fractions of up to 24%. These effects were enhanced in magnetic composites, possibly by dipole interactions. Mechanisms governing phase transitions triggered by NP loading in the interfacial instability process were proposed. The current study helps establish and elucidate the active role played by NPs in directing block copolymer assembly in the interfacial instability process, and provides important guiding principles for the use of this approach in generating NP-loaded block copolymer composites.

## Introduction

Because of their exceptional optical, electronic, chemical, and magnetic properties resulting from their small size, nanoparticles (NP) have wide ranging applications, including personalized medicine[1,2], alternative energy[3], and nano-catalysis[4]. Their small size, however, also increases aggregation kinetics, which can result in alteration or loss of the desired properties[5]. Furthermore, many widely-used and reliable NP synthesis protocols[6,7] employ hydrophobic solvents. For applications requiring aqueous solubility, particles must undergo a phase transfer, a process that can cause irreversible deterioration in NP properties[8]. Finally, many useful NPs are toxic, thereby limiting their use in biological environments[9]. Thus, methods to protect the surfaces of NP are required to maintain size-enabled properties, prevent aggregation, and reduce toxicity[10].

Common approaches to surface protection include ligand exchange[11], silica encapsulation[12], modification with amphiphilic polymers[13], and micelle encapsulation[14]. Among these, encapsulation within amphiphilic block copolymer (BCP) micelles is a popular choice because of the ability to protect large numbers of NPs within the micelle core[15-20]. In BCP micelles, the hydrophobic core serves as a reservoir for encapsulating hydrophobic cargo, whereas the hydrophilic shell protects the core and disperses the micelles in aqueous media[21]. The dominant approach for BCP micelle synthesis is the co-solvent addition method. In this method, BCPs and NPs are dispersed in a water-soluble, organic solvent. The solvent quality is then altered by water addition, inducing precipitation of the BCP hydrophobic block and the NPs[22]. When the precipitation rates of the BCPs and NPs are carefully matched, loaded micelles can form.

Unfortunately, the co-solvent addition method presents several challenges for NP encapsulation. NPs with sizes larger than the BCP radius of gyration can aggregate, inducing phase-separation within the system[23]. Further, prior modification of the NP surface with ligands compatible with the BCP is often required to promote encapsulation. However, surface modification can alter NP morphology and surface-derived properties, such as fluorescence[8]. Also, encapsulation of NPs within non-spherical micelles can be extremely difficult[24-26].

a. William G. Lowrie Department of Chemical and Biomolecular Engineering, The Ohio State University, 151 W. Woodruff Ave., Columbus, OH 43210, USA.
b. Department of Biomedical Engineering, The Ohio State University, 151 W. Woodruff Ave., Columbus, OH 43210, USA.
c. Department of Chemistry and Biochemistry, The Ohio State University, 151 W. Woodruff Ave., Columbus, OH 43210, USA.
Electronic Supplementary Information (ESI) available: Supplementary Figures. See DOI: 10.1039/x0xx00000x

Thus, the co-solvent addition method presents limitations in the size and surface chemistry of NP employed and the resultant micelle shapes that can be successfully processed.

Recently, the 'interfacial instability' approach has shown promise in achieving high NP encapsulation efficiency in micelles, without requiring prior modification of NP surface chemistry[16,17,24,25,27-30]. In the interfacial instability method[24], an organic, water-immiscible solvent containing the BCP and hydrophobic NPs is emulsified with water, aided by an aqueous phase surfactant. The aqueous phase surfactant and BCP adsorb on the emulsion droplet surface, dramatically reducing the interfacial tension. As the interfacial tension approaches zero, the emulsion droplets undergo repeated fission cycles. Simultaneously, the volatile organic solvent continues to evaporate, until the critical micelle concentration (CMC) is reached and NP-loaded micelles form.

Although the mechanism of interfacial instability has been described and explored[1,31], few reports have examined the influence of NP properties, including size, shape, and concentration, on the resultant composite morphology[29]. Anecdotally, we have observed that NP shape can alter micelle morphology[16,19], with non-spherical NPs decreasing NP packing and altering micelle morphology toward non-spherical shapes. Nie et al. found that increasing NP weight fraction triggered morphological phase transitions, altering micelle morphology from cylindrical worms to vesicles[29]. Upon increasing NP weight fraction further, spherical aggregates formed, which were prone to precipitation. These findings suggest that NP encapsulants play a pivotal role in micelle assembly in the interfacial instability process. Yet, the mechanism of NP-induced phase transitions, the impact of NP size and chemistry on phase transitions, and the limits of NP encapsulation within micelles are far from understood.

This study evaluates the influence of increased NP concentration on the shape and polydispersity of polymer nanocomposites synthesized via the interfacial instability approach. Poly(styrene-b-ethylene oxide) (PS-b-PEO) block co-polymers were employed as a model system because of their extensive use for NP encapsulation by our group[16,17,19,32] and others[24,33,34]. Additionally, two types of NPs, quantum dots (QDs) and superparamagnetic iron oxide nanoparticles (SPIONs), were investigated. QDs have been widely used for multicolour labelling assays and optical tracking[17,35-37]; however, maintenance of fluorescence properties upon aqueous transfer can be challenging[8]. Similarly, SPIONs have potential clinical applications as MRI contrast agents[15], hyperthermia mediators[38], integrated delivery systems activated by magnetic fields[39], and in cell separations[40]. Relevant to this study, SPIONs exhibit strong inter-nanoparticle magnetic dipole/dipole interactions[41] that may influence aggregation kinetics.

Using these materials, micelle size, polydispersity, shape, and NP packing were evaluated as a function of NP loading.

Polydispersity and morphology were examined using transmission electron microscopy (TEM) and image analysis. Complementary small angle X-ray scattering (SAXS) experiments were used to confirm the TEM results and to evaluate NP ordering and loading within densely-loaded composites. Results were compared for SPION- and QD-loaded composites to identify the potential role of NP interactions (e.g., dipole coupling) in assembly. In addition, for QD-loaded composites, fluorescence properties were investigated to identify potential relationships between micelle morphology and retention of NP properties. These data were used to suggest a potential mechanism of composite formation, in which morphology is dependent on NP concentration.

## Materials

Carboxyl-terminated poly(styrene-block-ethylene oxide, $PS_{90}$-b-$PEO_{400}$ ) (Cat No. P5755-SEOCOOH) was purchased from Polymer Source Inc. (Montreal, Canada). Poly(vinyl alcohol) (PVA) (cat no. 363170) was purchased from Sigma Aldrich. Chloroform (cat no. C606SK-4) was purchased from Fisher Scientific. Organic quantum dots (QDs), Qdot® 605 ITK™ (cat no. Q21701MP) with emission maxima of 605 nm ca. were purchased from ThermoFisher Scientific, MA. QDs consisted of a CdSe core with a ZnS shell and a surface coating of trioctylphosphine oxide (TOPO) coordinating ligands; QDs were supplied by the manufacturer in decane. SPIONs (Cat No. SOR-05-50) were purchased from Ocean NanoTech, CA, were composed of $Fe_2O_3$ with a surface coating of oleic acid, and were supplied by the manufacturer in chloroform.

## Methods

### Flocculation of QDs from Decane

QDs were supplied by the manufacturer dispersed in decane. However, chloroform is the preferred organic solvent for micelle synthesis via the interfacial instability method[42]. Thus, prior to micelle synthesis, QDs were transferred into chloroform using a flocculation procedure modified from that provided by the manufacturer. Briefly, a 100 µL suspension of QDs in decane at 1µM was mixed with 450 µL of a 2:1 (v/v) methanol: iso-propanol mixture. This solution was centrifuged at 4000 rcf for 3 minutes to precipitate the QDs. The supernatant was discarded and the QDs were briefly dried for 10 minutes before being resuspended in chloroform.

### Synthesis of NP-loaded PS-PEO micelles

PS-b-PEO, QD, and SPION stock solutions were prepared at fixed concentrations of 1 mg/mL, 0.4 µM, and 2.5 mg/mL in chloroform, respectively. PVA (aqueous-phase emulsifier) stock solution was prepared by mixing PVA at a concentration of 5 mg/mL in water. An organic phase was prepared with NP:PS-b-PEO mole ratios (based on particle number) of 0.005, 0.01, 0.025, 0.05 and 0.1 by adding corresponding volumes of

the NP stock solution (QD or SPION) to a fixed amount of PS-b-PEO (1 mg/mL, 100 μL) in chloroform. For the SPIONs, two additional NP:PS-b-PEO mole ratios, 0.25 and 1, were also prepared. This organic phase was then added to a fixed amount of PVA (5 mg/mL, 3 mL). The resulting bi-phasic solutions were sonicated in centrifuge tubes with an internal diameter of 1.7 cm, and submerged in a bath sonicator (Cole-Parmer, EW-08895-16) for an hour. The emulsions were transferred to aluminium dishes with an internal diameter of 5 cm and placed on a rocker to allow chloroform to evaporate. After roughly 2.5 hours, the initially opaque solutions became transparent, indicating the formation of nano-sized assemblies via the interfacial instability mechanism[24]. Process reproducibility was verified by synthesizing and analysing multiple samples (N $\geq$ 2) at the same NP-loading conditions (Supplemental Figure 1).

### Transmission Electron Microscopy (TEM)

NP-loaded composites were imaged using an FEI Tecnai G2 Bio Twin TEM. Sample droplets (20 μl) were placed on clean silicone pads, and TEM grids (Formvar/carbon coated nickel) were placed on these droplets carbon side down. After 3 minutes, the TEM grids were lifted, and excess solution was gently drained away with filter paper by capillary action. As the polymers (PS-b-PEO and PVA) have low electron densities, negative staining with Uranyl acetate (UA, 1%, 20 μl) was performed to improve image contrast. Excess UA was wicked away after 30 seconds.

### Image Analysis of Composite Morphology

Following TEM, images were assessed using ImageJ[43] image analysis software. For each image, the particle aspect ratio (AR) and thickness were measured until 100-2000 total composites were quantified. Thickness, defined as the maximum distance perpendicular to the axial direction, was used as a surrogate for diameter. For spherical micelles, the thickness is simply the diameter; and for elongated micelles, it is the diameter of the cylindrical portion. Size distribution

histograms were constructed using Igor Pro 6.37 software (Wavemetrics, OR). Data were fit using the Gaussian function, and the mean size and standard deviation were extracted. Particle aspect ratio was used to classify micelles as spherical (AR $\leq$ 1.2) or elongated (AR > 1.2). Densely-loaded structures, much larger than the spherical micelles, were identified by visual inspection.

### Small Angle X-ray Scattering (SAXS)

SAXS experiments on NP-loaded PS-PEO composites were performed at the Advanced Photon Source, Argonne National Labs, Argonne, IL using the 12-ID-C beam line[44]. Spectra were collected using an incident X-ray of wavelength 0.1 nm and a scattering wave-vector range of 0.005 Å$^{-1}$ < Q < 0.6 Å$^{-1}$. SAXS was performed on dilute solutions of NP-loaded composites suspended in aqueous emulsifier (PVA) and loaded in a quartz capillary. The background was the same capillary filled with distilled water. The PS-b-PEO concentration was equal to 0.001 mg/mL in of each of the samples. The two-dimensional scattering patterns were reduced to generate one-dimensional scattering spectra using the APS software. Scattering spectra were fit using the SasView program[45].

### Statistics

Statistical analyses were performed using JMP Pro 12 software (SAS Institute Inc., Cary, NC, USA) via the ANOVA test for samples with Gaussian distribution. P-values of <0.05 were interpreted as statistically significant.

### Fluorescence spectroscopy

Fluorescence spectra of the QD-loaded composites were collected using a Perkin Elmer fluorometer LS 45. QD-composite samples were excited by laser irradiation at 350 nm and emission spectra were recorded between 565 nm and 645 nm. Sample fluorescence was compared using peak heights at ~605 nm. Composite stability was assessed by performing fluorescence measurements in triplicate over 7 days.

## Results and Discussion

### Nanoparticle characterization

Previous anecdotal evidence[15,16,19] suggests that NP shape can influence NP packing within micelles and composite micellar morphology. Thus, we first evaluated the shape (aspect ratio, AR) and size (thickness, a surrogate measure of diameter) of the NP encapsulants (Figure 1). The QDs employed in this study exhibited slightly elongated shapes (Figure 1A,B), with a mode AR > 1 (where AR = 1 for spheres). Thickness exhibited a Gaussian distribution with a mean of 6.0 $\pm$ 1.5 nm (Figure 1C). In contrast, SPIONs were spherical with ARs closer to 1 (Figure 1D,E) and thicknesses of 5.1 $\pm$ 0.5 nm (Figure 1F).
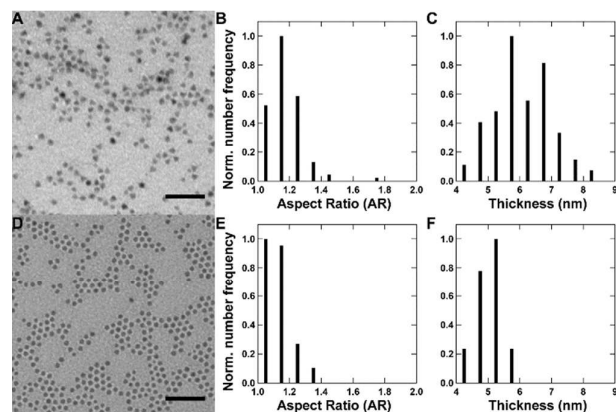


Figure 1: Size characterization of QD and SPION encapsulants used for preparing composites: QD (A) TEM images, (B) Aspect Ratios (ARs), and (C) Thickness size distribution and SPION (D) TEM images, (E) Aspect Ratios, and (F) Thickness size distributions. (A,D) Scale bar = 20 nm.

### Characterization of Unloaded, Control PS-b-PEO micelles

Next, as a control, the size of empty micelles without NP encapsulants was evaluated. In the absence of NP encapsulants, $PS_{90}$-b-$PEO_{400}$ BCPs (weight fraction PEO block=0.65) assemble into spherical micelles at the concentrations and temperatures employed[25,46] (Figure 2). Specifically, unloaded, control PS-b-PEO micelles displayed a mode AR of 1.03, consistent with a spherical morphology. Roughly 95% of the micelles exhibited ARs < 1.2 (Figure 2B). Control, unloaded PS-b-PEO micelles exhibited mean sizes of 32.3 ± 9.5 nm (Figure 2C), in agreement with the literature[46].
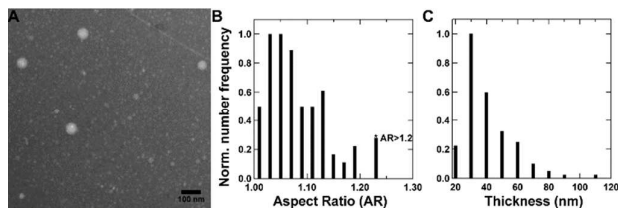


Figure 2: Size characterization of unloaded, control PS-b-PEO micelles without NP encapsulants: (A) TEM images, (B) Aspect Ratios, and (C) Thickness size distribution. Scale bar = 100 nm.

### Effect of NP loading on micelle morphology

Next, micelles with NP encapsulants were generated using NP:PS-b-PEO mole ratios ranging from 0.005 to 1. For QD:PS-b-PEO mole ratios above 0.1, the final solution remained opaque and large secondary aggregates were seen (Supplemental Figure 2), indicating failed assembly. Thus, QDs NP:polymer ratios above 0.1 were not investigated further. In contrast, SPION composites were successfully synthesized across the
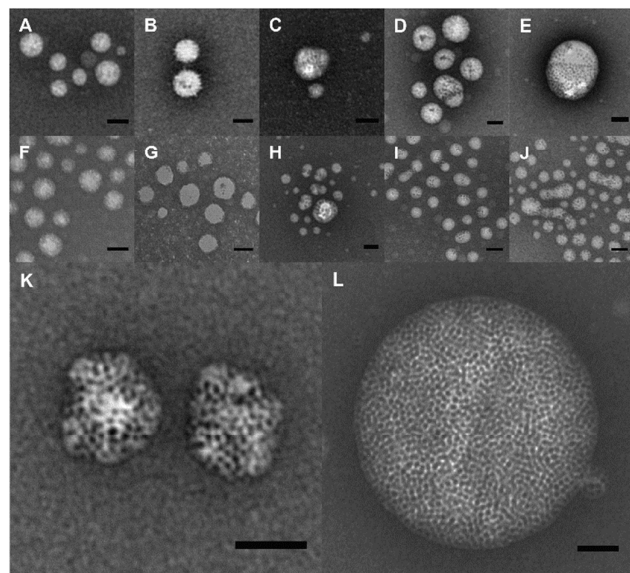


Figure 3: TEM images of micelles with increasing NP:PS-b-PEO mole ratio: QD (A-E) and SPION (F-J) micelles at mole ratios of (A, F) 0.005, (B, G) 0.01, (C, H) 0.025, (D, I) 0.05, and (E, J) 0.1, respectively. (K, L) Densely-loaded NP/PS-b-PEO structures: (K) QDs at QD:PS-b-PEO=0.1 and (L) SPIONs at SPION:PS-b-PEO=1. Scale bar = 50 nm.

entire range of ratios. Increasing NP encapsulant concentration induced morphological transitions and the appearance of densely-loaded structures as seen in TEM (Figure 3), as quantified by AR (Figure 4), and as summarized schematically in Figure 5. Specifically, increasing NP concentration increased the number elongated micelles relative to unloaded, control PS-b-PEO micelles. In addition, above a critical mole ratio (~ 0.025), densely-loaded structures (Figure 3K,L) appeared. These densely-loaded structures had markedly higher NP densities than the spherical and elongated micelles observed at lower mole ratios. Interestingly, these phase transitions were seen for both types of NP encapsulants investigated, and, for SPIONs, densely-loaded structures became the dominant morphology at higher mole ratios.

These results are consistent with previous observations. Increasing polymer concentration, temperature, or BCP hydrophobic block weight fraction, can all influence unloaded micelle morphology, driving the formation of higher order structures, such as the elongated micelles observed here[22,47,48]. In the co-solvent method, the effect of nanoparticle concentration on micelle morphology has been studied by several groups[49-51]. For example, Park et al. suggested that NPs can increase the effective volume of the BCP selective block during micelle formation[50]. In general, increasing the effective BCP hydrophobic content triggers phase transitions from spherical to cylindrical micelles in the co-solvent method.

The interfacial instability method used here is mechanistically distinct from the co-solvent method in several key aspects. In the interfacial instability method, BCP assembly and, ultimately micelle phase, is controlled by a complex interplay of confinement effects, interfacial forces, and supramolecular forces of attraction[25]. As described by Hayward et al., the interfacial instability mechanism is influenced by BCP hydrophobic content[24,25]. Experimentally, BCPs with low hydrophobic content have been shown to trigger droplet fission into smaller droplets with subsequent assembly into spherical micelles, whereas BCPs with intermediate hydrophobic content result in the ejection of fluid tendrils that assemble into cylindrical or worm-like micelles. The observation of elongated micelles in our system, even at relatively low NP ratios, indicates that NPs can impact the interfacial instability mechanism (Figure 5A,B). NPs interact with the hydrophobic BCP block through specific intermolecular forces including hydrogen-bonding, electrostatic, and van der Waals forces[52]. As these forces are strongly distance dependent, shrinking emulsion droplets can facilitate and enhance favourable BCP-NP enthalpic interactions, increasing the effective hydrophobic content of the BCP and triggering phase transitions that resemble those in BCP micelles as the hydrophobic block is increased.

Similarly, the hydrophobic ligands on the NP surface also add to the effective hydrophobic content of the BCP. Surface ligands leaching from the NP surface may become entrapped
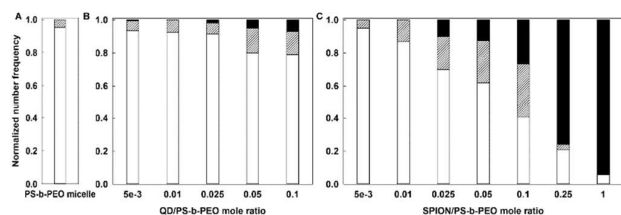
Figure 4: Normalized number frequency of micellar morphologies for (A) control, unloaded micelles and micelles with (B) QD and (C) SPION encapsulants. Spherical micelles (ARs < 1.2) = white bars, elongated micelles (ARs > 1.2) = dashed bars, densely-loaded structures (TEM visualization) = black bars. (100 < N < 2000).

within the micelle core. Leached surface ligands would behave as hydrophobic polymer encapsulants within the micelles, similar to drug delivery molecules, and could also contribute to phase transitions[22].

Extending this analysis to the densely-loaded structures observed at high NP:polymer mole ratios (Figure 3K-L, Figure 4), several possible mechanisms are considered. Although it is possible that these densely-loaded structures could consist of micelles with multiple NPs tightly packed in their cores, this would require substantial stretching of the PS block, which is unlikely. PS-b-PEO micelles are kinetically frozen at room temperature because of the high glass transition temperature of the PS block (~100 °C)[53]. Thus, such stretching would induce a loss in conformational entropy and is permitted only to a finite extent[21,22]. A more likely possibility is that densely-loaded structures are the result of NP aggregation followed by stabilization via PS-b-PEO adsorption (Figure 5C). As the NP concentration within the emulsion droplet increases, the probability of NP-NP association would be expected to increase correspondingly. Indeed, aggregation of NPs as a result of charge screening and Van der Waals attractions is widely known[54]. As the interfacial tension at the surface of the emulsion droplet approaches zero, NP aggregates could be ejected. The BCP in the droplets would then precipitate onto the surface of the NP aggregates, stabilizing the cluster and effectively arresting further growth. The nearly spherical geometry of the final structures in this case would be driven by the preferred packing dimensions of the NPs (i.e., typically close-packed spheres for spherical NP geometries), although the preferred BCP curvature may also play a role.

To evaluate these possibilities, synthesis was repeated under the same conditions as those used to generate Figure 3L, but in the absence of BCP (Supplemental Figure 3). Dense NP structures were observed even in the absence of BCP, suggesting that these structures are not higher-order micellar structures, but are most likely polymer stabilized NP-aggregates. These data suggest the presence of a critical NP:BCP mole ratio for the interfacial instability method, beyond which micelle formation likely no longer occurs, and BCP stabilized NP aggregates are favoured. Further, in the absence of BCP, both spherical and raft aggregates were observed, whereas the majority of densely-loaded structures observed in the presence of BCP were spherical (93% of the
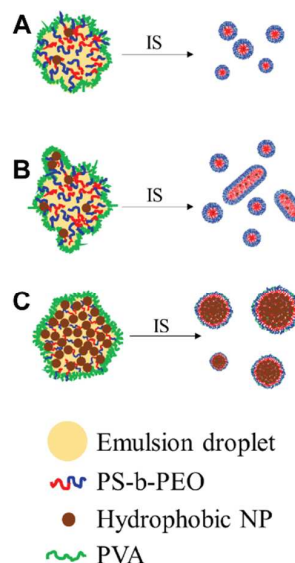


Figure 5: Proposed Mechanism of phase transitions triggered by NP loading in PS-b-PEO micelles. (A) Low NP content (NP:PS-b-PEO mole ratio < ~0.01) results in the parent emulsion droplet ejecting smaller, spherical daughter droplets, similar to unloaded controls. (B) Moderate NP content (0.01 < NP:PS-b-PEO mole ratio < 0.025) results in the parent emulsion droplet ejecting some fluid tendrils that lead to the formation of elongated structures. (C) At high NP content (NP:PS-b-PEO mole ratio > 0.025), some BCP-stabilized, densely-loaded NP structures form.

structures have ARs < 1.2). This suggests that the BCP plays an important role in directing NP aggregate assembly and stabilization. Future work should include polymers with differing geometries and more asymmetrical NPs to further explore these possibilities.

**Effect of NP loading on micelle size and polydispersity**

Next, the effect of NP loading on composite size and size distribution was examined. NP-BCP composite sizes varied by morphology (Table 1). Mean diameters for spherical micelles were ~ 25-40 nm for both NP encapsulants. This is not surprising as the size of spherical micelles is tightly controlled by the ability of the PS block to stretch. As maximum stretching for the core block is reached, spheres will transition to cylinders[55]. This is consistent with the observed formation of elongated micelles as NP loading was increased (e.g., Figure 4).
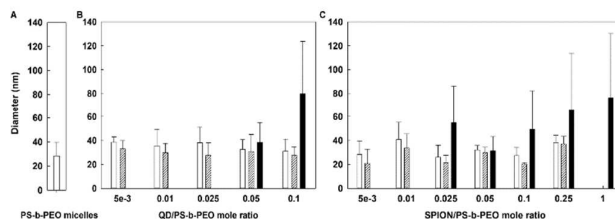


Figure 6: Mean thickness of (A) control, unloaded PS-b-PEO micelles and micelles encapsulating (B) QDs or (C) SPIONs. White = spherical micelles, grey hashed = elongated micelles, and black = densely-loaded structures. Error bars represent standard deviation.

Elongated micelles exhibited thicknesses of ~ 20-40 nm, generally smaller than that observed for spherical micelles under the same conditions (Figure 6, Table 1, $p < 0.05$ except SPION 0.05 sample), and variable lengths (Supplemental Figure 4). It has been previously reported that elongated micelles have a lower degree of stretching in the radial direction compared to spherical micelles. Because elongated micelles have an additional degree of growth along their axis, they can increase their hydrophobic core volume axially, without increasing in diameter[22]. This may explain the smaller thickness of elongated micelles compared to spherical micelles observed in most conditions.

In contrast to spherical and elongated micelles, densely-loaded structures exhibited large variations in size. As densely-loaded structures are most likely polymer-stabilized NP aggregates, their size would depend on NP aggregation kinetics, as well as the time required for stabilization by BCP adsorption. During the interfacial instability process, local inhomogeneity may persist in emulsion droplet size. This could result in non-uniform NP aggregation within the droplets and thereby lead to the broad size distribution observed in the final structures.

Table 1: Mean ± std. dev. of thicknesses by morphology at different NP loadings. *Number of structures observed was too small for statistically relevant quantification.

| NP:PS-b-PEO mole ratio | Spherical micelles | Elongated micelles | Densely-loaded structures |
|---|---|---|---|
| **Empty micelles** | | | |
| 0 | 32.3 ± 9.5 | * | * |
| **QD-series** | | | |
| 0.005 | 38.5 ± 4.4 | 33.0 ± 7.0 | * |
| 0.01 | 35.5 ± 13.8 | 29.7 ± 7.8 | * |
| 0.025 | 38.0 ± 13.0 | 27.5 ± 10.3 | * |
| 0.05 | 32.4 ± 8.4 | 30.7 ± 14.3 | 38.4 ± 16.4 |
| 0.1 | 31.0 ± 10.2 | 27.5 ± 7.2 | 79.7 ± 44.0 |
| **SPION-series** | | | |
| 0.005 | 28.3 ± 11.2 | 21.0 ± 11.7 | * |
| 0.01 | 40.8 ± 14.4 | 33.7 ± 11.7 | * |
| 0.025 | 26.0 ± 10.0 | 21.3 ± 6.4 | 54.7 ± 31.6 |
| 0.05 | 32.0 ± 3.7 | 29.9 ± 4.4 | 31.5 ± 11.8 |
| 0.1 | 27.4 ± 6.8 | 20.4 ± 1.3 | 49.3 ± 32.9 |
| 0.25 | 38.2 ± 6.2 | 37.0 ± 6.4 | 65.6 ± 48.1` |
| 1 | * | * | 76.3 ± 54.0 |

### Nanoparticle packing inside densely-loaded structures

Given the densely-loaded structures observed at higher NP:PS-b-PEO mole ratios, the effect of increasing this ratio on internal NP ordering and packing volume fraction was evaluated semi-quantitatively. Previously, we[16] and others[15] have observed potential differences in NP packing and ordering based on encapsulant shape in TEM images. For example, more elongated NPs generally produced micelles containing larger regions devoid of particles than did spherical NPs. To quantify this difference, we turned to small-angle X-ray scattering (SAXS). Here, ordering of encapsulated NPs within densely-loaded structures should be characterized by scattering spectra that require structure factors. Incorporating the structure factor into the fit should then yield an estimate for the volume fraction of particles within the densely-loaded structure.

Table 2: X-Ray Scattering Length Densities (SLD) of species in solution calculated using Scattering Length Density calculator[56]

| Species | Material | Density (g/mL) | SLD ($10^{-6}$/Å$^2$) |
|---|---|---|---|
| SPIONs | $Fe_2O_3$ (core) | 5.24 | 41.125 |
| QDs | CdSe (core) | 5.82 | 41.992 |
| PS | $(C_8H_8)_n$ | 1.04 | 9.516 |
| PEO | $C_{2n}H_{4n+2}O_{n+1}$ | 1.21 | 11.295 |
| PVA | $(C_2H_4O)_n$ | 1.19 | 11.044 |
| $H_2O$ | $H_2O$ | 1.00 | 9.469 |

As noted in Table 2, the scattering length densities (SLD) of PS, PEO, PVA, and $H_2O$ are all very close, whereas both types of NPs have much higher SLD. Unfortunately, in many of the SAXS experiments, the PS-b-PEO concentration used (0.001 wt.%) was too low and the PVA concentration was too high (0.5 wt.%) for the empty and lightly loaded micelles to be detected above the solution background. Consequently, the scattering spectra of the micelles with low NP:PS-b-PEO ratios overlap almost entirely with the scattering spectra of the PVA solution (Figure 7A,B).

In contrast, at high NP:PS-b-PEO mole ratios (e.g., 0.1 and 1 for the QD-and SPION-micelles, respectively), the scattering spectra (Figure 7A,B) exhibited features distinct from the PVA background, including a strong increase in the scattering signal for $0.05 < Q$ /$\text{Å}^{-1}< 0.1$, i.e. at length scales consistent with the size of the NPs. These scattering spectra correspond to conditions at which densely-loaded structures are observed (Figure 3K,L), and thus may be attributed to scattering from the NPs within them. The appearance of these features in the scattering spectra of the densely-loaded samples suggests that the densely-loaded structures exist throughout the solution and are not limited to a few anomalous composites observed via TEM.

To analyse the scattering spectra of the densely-loaded structures further, we first subtracted the PVA solution signal from the highest NP:PS-b-PEO scattering curves. The remaining signal (Figure 7C,D) consists of a power law region at low Q due to the presence of larger structures, and a signal at $Q > 0.05$ $\text{Å}^{-1}$ due to scattering from the NPs within the structures. In the case of the QDs, the slope of the power law is -2.6, consistent with mass fractals. By subtracting this power law, we further isolated the signal resulting from the NPs and fit this curve to a polydisperse (lognormal) distribution of spheres including a hard sphere structure factor (Supplemental Figure 5). The fit provides estimates for the size and polydispersity of NPs forming the densely-loaded structures, as well as the volume fraction of particles within them. Fitting the SPION sample was more challenging, in part because the power law region has two slopes. The slope at lower Q ($0.006 < Q$ /$\text{Å}^{-1} < 0.015$) is ~ -1.8, characteristic of diffusion limited aggregates. The slope at intermediate Q ($0.015 < Q$ /$\text{Å}^{-1} < 0.03$) is more difficult to estimate because these data contain contributions from the NPs as well as the aggregates or the structures that formed the aggregates. Nevertheless, for $Q > \sim0.05$ $\text{Å}^{-1}$ scattering should be dominated by the NPs and this region of the spectrum is well fit by a polydisperse (lognormal) distributions of spheres with a hard core structure factor (Supplemental Figure 6). Table 3 summarizes these fit results.
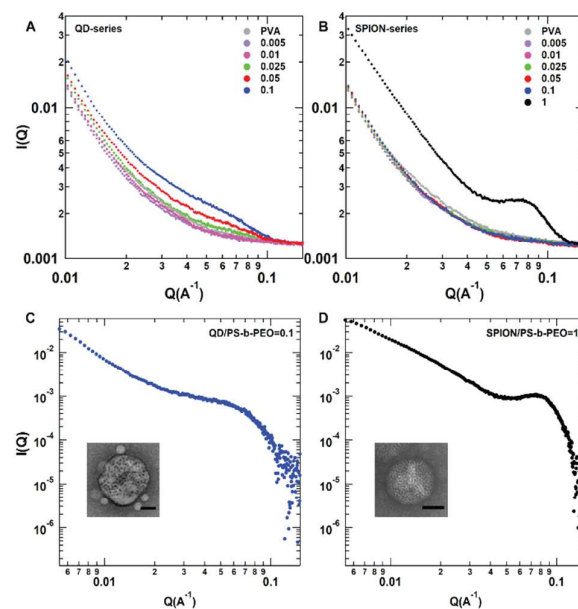


Figure 7: Small Angle X-ray Scattering (SAXS) spectra measured as a function of the momentum transfer vector $Q=(4\pi/\lambda)$ sin$(\theta/2)$, where $\lambda$ is the wavelength of the incident radiation and $\theta$ is the scattering angle.  (A) QD- and (B) SPION- loaded micelles. (C, D) Subtracting the PVA spectra for (C) QD:PS-b-PEO=0.1 and (D) SPION:PS-b-PEO=1 enhances the features present at higher Q. Inset: TEM image of representative structure from each sample. Scale bar = 50 nm.

Fitting the SAXS data yielded average NP sizes, relative NP distribution widths, and particle loading parameters that are quite consistent with the TEM images. In particular, the average particle size is within 1 nm of that observed by TEM, the particle size distribution for QDs is broader than that for SPIONS, and the packing fraction for SPIONS is higher than that for QDs. Although TEM suggests the QDs are slightly asymmetric, fitting the SAXS data to ellipsoids or cylinders did not change the results qualitatively. Combining the volume fraction of NPs derived from SAXS with the size of the densely-loaded structure from the TEM images, we estimated the average number of NPs in a structure as

$$N_{NP}=\phi_{NP}(V_M/V_{NP}) \qquad \text{(Equation 1)}$$

where $\phi_{NP}$ is the volume fraction of NPs derived from SAXS, $V_M$ is the volume of the micelle structure based on TEM size measurement, and $V_{NP}$ is the NP volume based on TEM size measurement.

Table 3: Fit parameters corresponding to NPs within densely-loaded structures. The estimated number of NPs in each structure is based on the TEM values for NP and structure size (Figure 6) and the volume fraction determined by SAXS.

|  | QD:PS-b-PEO=0.1 | SPION:PS-b-PEO=1 |
| --- | --- | --- |
| NP diameter from SAXS fits(nm) | 6.2±1.2 | 6.2±0.6 |
| Volume fraction of NPs in structure | 0.13 | 0.24 |
| Average Centre-to-Centre Spacing between NPs (nm) | 13 | 7.4 |
| Average Number NPs ($N_{NP}$) in an 80 nm structure | ~200 | ~900 |

To calculate the maximum number of NPs ($N_{NP}$) in the densely-loaded structures (Table 3), we assumed the structures were spheres with diameters of 80 nm. For $V_{NP}$, we used the sizes determined from TEM analysis. In particular, SPIONs are spheres with average diameters of 5.1 nm and QDs are cylinders with average diameters of 6 nm and lengths of 7.2 nm. Solving Equation 1 suggests that, for the densely-loaded structures in Figure 7, the average number of SPIONs is more than 4 times the average number of QDs. These differences are consistent with the higher SPION:PS-b-PEO loading, the TEM observations for the densely-loaded QD and SPION structures (Figure 3), and anecdotal observations of less dense packing for non-spherical NPs[15,16].

Likewise, if we assume that particles are evenly distributed throughout the densely-loaded structures, then the maximum volume occupied by each particle, assuming hexagonal close packing of spheres, is given by:

$$V_{NP,max}=0.74(V_{NP}/N_{NP}) \qquad \text{(Equation 2)}$$

The diameter corresponding to this spherical volume, in turn, yields the average distance between NPs (centre to centre) (Table 3). Thus, assuming spherical shape and a diameter of ~5.1 nm as measured in TEM; SPIONs are separated by ~ 2 nm (edge-to-edge). For QDs, which are assumed cylindrical with dimensions 6 nm x 7.2 nm, this represents a separation of ~ 6-7 nm depending on orientation. The distance derived using this simple picture is quite consistent with the TEM images of densely-loaded SPION structures, although it is impossible to directly quantify 3D distances on 2D TEM images. It is less consistent with the TEM images of densely-loaded QD structures because these also have large regions devoid of NPs.

**Differences in Morphology and NP Packing in Densely-Loaded Structures**

The QDs had ARs of 1-1.5, indicating a slightly more rod-like structure than SPIONs. However, these NPs were confined into roughly spherical structures by the BCP's preferred curvature. Bockstaller et al. report that rod-like/cylindrical NP encapsulants and spherical host domains are a geometrically incompatible pair[56]. Geometric dissimilarity between the entrapped NPs and the host BCP domains can result in a greater entropic penalty and morphological defects in the resulting composite. This is evident in the morphology of the densely-loaded QD structures, which reveals rough, uneven surfaces (Figure 3K, Figure 7C, inset). This is also consistent with our previous observations of "lumpy" micelle formation during encapsulation of NP tetrapods[19]. In comparison, the shape of the scattering curve for the densely-loaded SPION structures suggests a higher degree of order within these micelles. Visual observation confirms that the surfaces of these structures were also more uniformly smooth and NPs appear more tightly packed (Figure 3L, Figure 7D, inset).

Densely-loaded structures of QDs and SPIONs display differences in relative morphology distribution (Figure 4), mean size (Table 1), and NP packing (Table 3). There are several possible causes for these morphological differences. First, the structures were produced using different mole ratios (i.e., mole ratios of 0.1 for QDs vs. 1 for SPIONs), thus the NP loadings of the structures analysed here are expected to differ. The use of different mole ratios was, however, driven by two factors: stable QD composites could not be synthesized at mole ratios > 0.1 (Supplemental Figure 2) and densely-loaded SPION structures did not display scattering above that of PVA at such a low mole ratio. This suggests that differences in NP: PS-b-PEO mole ratio alone are not responsible for observed morphological differences.

One possibility is that these differences originate from different NP surface chemistries. Surface chemistry strongly influences encapsulation. For example, in studies of drug encapsulation, drugs that are chemically more similar to the host polymer matrix, undergo higher encapsulation[57]. The NPs evaluated were coated with TOPO (QDs) and oleic acid (SPIONs). To evaluate the potential differences imparted by surface chemistry, solubility parameters, $\delta$, were calculated for the chemical species most likely to interact in this system. Parameters were calculated using the Hildebrand method[58], in which species that display similar values are more likely to interact with each other. In this case, $\delta$ for oleic acid (i.e., the coating on SPIONs) differs by 1.4 from that of the PS block, whereas $\delta$ for TOPO (i.e., QDs) differs by 1.3. These differences are sufficiently close that ligand-BCP interactions alone are unlikely to strongly contribute to differences in nanoparticle encapsulation. [It is noted that the difference in $\delta$ between PVA and TOPO is smaller than between PVA and Oleic Acid, which may result in some increase in undesired QD-PVA binding. Nonetheless, PVA displays far less affinity for TOPO surfaces than PS, based on this method of evaluating compatibility.]

ARTICLE

Table 4: Solubility parameters by chemical species calculated by the method of Hildebrand.

| Chemical Species | Solubility Parameter $\delta$, $(J/cm^3)^{1/2}$ |
| --- | --- |
| Oleic Acid | 17.3 |
| TOPO | 20 |
| PVA | 32.9 |
| PS | 18.7 |

It is also possible that ligand density varies between NPs, which could provide an increase in effective hydrophobic content. Further investigation is needed to evaluate this possibility. However, this seems unlikely given that both particles have similar surface areas and demonstrate good initial colloidal stability, suggesting similar surface coverage.

It is more likely that ligand influences NP aggregation kinetics, and thus, the ability to nucleate and grow stable NP aggregate cores that are later passivated by BCPs. Indeed, ligand-ligand and ligand solvent interactions have been shown to dominate aggregation kinetics in assembly of gold NPs[59]. Surface ligand charge, molecular weight, and area density can impact NP distribution within micelles and NP aggregation kinetics[21]. The ligands utilized in this study, TOPO (QDs) and oleic acid (SPIONs), are conformationally distinct. TOPO has 3 alkyl chains, whereas oleic acid has 1 alkanoic chain. These molecules are believed to adopt different conformations on the NP surface, with TOPO lying primarily flat across the NP versus oleic acid extending linearly from the NP surface[60]. Further, although oleic acid should be uncharged when bound to the NP surface, we have anecdotally observed behaviour suggesting the capacity for charge repulsion, either resulting from free ligand or ligand that is loosely adsorbed to the NP surface. These differences in steric properties and/or charge repulsion may impact NP aggregation kinetics, leading to the observed behaviours.

An additional contributing factor is likely NP shape. Non-spherical particles, such as the QDs studied here (AR > 1), have been shown to aggregate at lower concentrations than spherical particles of similar volume[54]. When two particles interact at a distance less than their diameter, non-spherical particles exhibit greater attractive interactions because of their irregular distribution of mass, which places more atoms close to each other[54]. Additionally, cylindrical/rod-like particles favour alignment rather than random or cross-alignment to maximize interactions along their length. Further, Monte Carlo simulations show that confined polyhedra tend to order even in the absence of specific attractive interactions[61]. Configurations in which larger NP faces are aligned are energetically more favoured. Spherical confinement can force non-spherical polyhedra to pack in a method similar to spheres. Thus, the irregular shape of QDs most likely drives aggregation as a result of increased attractive forces, leading to the formation of densely-loaded structures at lower concentrations than those of SPIONs. However, packing is also less efficient, and thus densely-loaded structures exhibit larger

standard deviations in mean size and irregular shapes. Irregular shape may result from incompatibility with the BCP preferred curvature, which is spherical in this case.

Finally, SPION packing may be enhanced by strong inter-NP magnetic dipole/dipole interaction forces. These forces are relatively weak at distances > 5 nm for the ~ 5 nm particles employed here. Thus, they would not be expected to strongly contribute to particle aggregation in dilute solution. However, as the emulsion droplet shrinks, interparticle separation distance declines, increasing the probability of dipole interactions. In the tightly confined space of the micelle, particles are likely in sufficient proximity for dipole forces to enhance their interactions, reducing separation distance. Additional research is needed to distinguish possible contributions of NP ligand, shape, and dipole coupling in directing NP packing in BCP micelles.

### Fluorescence of QD-BCP composites as function of NP/PS-b-PEO mole ratio

Next, we investigated the effect of NP packing on particle stability using QDs as a model system. QDs are known to demonstrate variable stability because of oxidation and the formation of trapped states[62]. Further, in aqueous media, poorly protected QDs lose fluorescence rapidly because of irreversible damage to their surfaces[63]. In addition, QDs in close proximity can potentially interact with each other. Previously, we have shown that QD encapsulation in micelles can increase fluorescence intensity without significant increases in overall NP size[17,19], but the role of NP packing was not explored. Thus, the role of QD:PS-b-PEO ratio (and therefore packing) on fluorescence of the resulting micelles and densely-loaded structures was evaluated over 7 days. In this study, CdSe-ZnS QDs with an organic TOPO coating were employed, as these are the most commonly employed QDs in biological research.

Fluorescence intensity increased with QD loading (Figure 8) (i.e., QD:PS-b-PEO mole ratio in the original organic phase), and, furthermore, two distinct regions were evident: QD:PS-b-PEO ratio < 0.025 and > 0.025. The increase in fluorescence
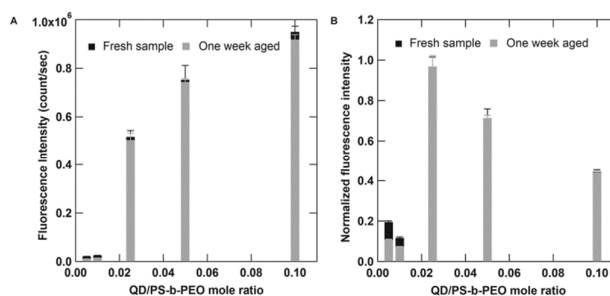


Figure 8: (A) Total fluorescence intensity of QD-micelles and densely-loaded structures as a function of QD:PS-b-PEO ratio in the organic phase and (B) as normalized to QD content. Black and grey bars represent the fluorescence intensity of fresh samples vs. those aged one week, respectively (N=5).

levels at QD:PS-b-PEO ratio > 0.025 is surprising as we would expect a simple linear relationship between fluorescence and QD-concentration in solution if NP loading in micelles occurred in a linear manner. These data indicate a possible relationship between fluorescence intensity and micellar morphology. At low NP ratios, fluorescence values were much lower. This region corresponds with micelle morphologies in which QD encapsulation is driven by PS block stretching and the number of encapsulated particles is likely low. At higher NP ratios, consistent with the appearance of densely-loaded structures (Figure 3K), a substantial increase in fluorescence is observed, corresponding to a large increase in the number of NPs encapsulated. This suggests that QD encapsulation can be tuned depending on the desired application: from single QD tracking applications to applications requiring high fluorescence intensity in a compact volume.

QD stability was also dependent on NP:PS-b-PEO ratio, and therefore loading, with a statistically significant decline over 1 week for lower NP:PS-b-PEO ratios (i.e., 0.005, 0.01), but no statistically significant decrease at the higher ratios. These differences correspond to micelles and densely-loaded structures, respectively. The fluorescence stability seen at higher NP:PS-b-PEO ratios suggests that densely-loaded structures can afford superior surface protection to QDs and that they are, in fact, a stable morphology. The observed decline in fluorescence for micelles may result from the smaller number of encapsulated QDs, with loss of signal of any one QD thus playing a larger role towards the integrated signal. Single particle measurements should be performed to evaluate this possibility. Alternatively, the densely-loaded structure morphology may provide additional surface protection because of the tight packing between particles. Fewer particles are closer to the micelle surface, reducing exposure to surface based phenomena.

These results are consistent with our prior observations that micelles can enhance and preserve the fluorescence of organic QDs[19]. However, we observed a maximum in QD intensity on a per QD basis at intermediate NP:PS-b-PEO ratios (i.e., 0.025) (Figure 8B), which has not been previously reported. It is unclear what the exact nature of the per particle fluorescence decline at higher NP:PS-b-PEO ratios results from. As this ratio represents concentration values in the original solution, reduced fluorescence could result from reduced QD encapsulation, perhaps as a result of the formation of unpassivated QD aggregates that segregate from solution. It is also possible that QDs lose fluorescence during micelle synthesis as a result of surface oxidation. However, this behaviour would be expected to inversely correlate with NP concentration, as increased numbers of NPs would drive more rapid aggregate formation reducing access to NP surfaces. The observation that fluorescence intensity remained stable for a week post synthesis indicates that the densely-loaded structures were stable post formation, even at high NP:PS-b-PEO mole ratios. This data argues against surface oxidation

post-synthesis as a possible cause of lower fluorescence on a per QD basis.

These data suggest that there is a critical NP:PS-b-PEO ratio in the interfacial instability method for optimum preservation of QD fluorescence. Interestingly, recent reports suggest that synthetic method (i.e., manual shaking vs. sonication) can also influence QD stability in BCP structures,[33] possibly through the formation of unstable PVA intermediates. These data suggest that initial formation of NP aggregates followed by polymer adsorption may be a favourable synthetic approach to highly stable QD nanocomposites.

## Conclusion

This study evaluated the role of NP:BCP ratio on composite morphology and NP packing in the interfacial instability process. QDs and SPIONs were employed as model NPs and encapsulated in PS-b-PEO BCPs. Depending on the NP:PS-b-PEO ratio, two different regimes were observed. At lower NP:PS-b-PEO ratios, spherical micelles were produced. As the ratio increased, spherical micelles underwent phase transformation to elongated structures, most likely to minimize BCP stretching. Thickness distributions for both spherical and elongated micelles were narrow, most likely as a result of BCP stretching limitations. However, beyond a critical NP concentration, a previously unknown morphology consisting of densely-loaded, ordered NPs within a polymeric coating formed. Densely-loaded structures had a broader size distribution (i.e., polydispersity). This suggests the possibility of two regimes in the interfacial instability process dominated by BCP vs. NP aggregation times, respectively. Interestingly, QD and SPION encapsulants exhibited different critical NP:PS-b-PEO mole ratios at which these transitions were observed. The difference may stem from differences in their surface chemistries, shapes, or interparticle interactions. Additional experiments with more controlled shapes and surface chemistries could differentiate these possibilities.

SAXS analyses confirmed the emergence of an ordered NP phase, corresponding to the densely-loaded structures. These densely-loaded structures had NP volume fractions of ~10-25%, with mean sizes < 100 nm, characteristics that could enable future use in a variety of applications. For example, magnetic particles used in cell separations typically display packing volumes of 5-10%[64], below the packing volumes observed here. Additionally, densely-loaded structures displayed higher retention of QD fluorescence over time than micelles with low NP encapsulation, indicating potentially different formation mechanisms and structures. These data indicate that the interfacial instability approach can lead to densely-loaded nanocomposites, although likely through an alternative mechanism in which NP aggregation precedes polymer aggregation. These studies thus highlight the importance of careful optimization of NP loading conditions to

obtain highly functional micelles with low morphological and size diversity.

## References

1    Zhu, J. T. & Hayward, R. C. Spontaneous generation of amphiphilic block copolymer micelles with multiple morphologies through interfacial instabilities. *J. Am. Chem. Soc.* **130**, 7496-7502 (2008).

2    Jain, K. K. in *Nanoparticles in Translational Science and Medicine* Vol. 104 *Progress in Molecular Biology and Translational Science* (ed A. Villaverde)  325-354 (2011).

3    Zhang, H.-w., Liu, Y. & Sun, S.-h. Synthesis and assembly of magnetic nanoparticles for information and energy storage applications. *Frontiers of Physics in China* **5**, 347-356, doi:10.1007/s11467-010-0104-9 (2010).

4    Kim, T., Fu, X., Warther, D. & Sailor, M. J. Size-Controlled Pd Nanoparticle Catalysts Prepared by Galvanic Displacement into a Porous Si-Iron Oxide Nanoparticle Host. *ACS Nano* **11**, 2773-2784, doi:10.1021/acsnano.6b07820 (2017).

5    Zhang, W. Nanoparticle Aggregation: Principles and Modeling. *Nanomaterial: Impacts on Cell Biology and Medicine* **811**, 19-43, doi:10.1007/978-94-017-8739-0_2 (2014).

6    Peng, Z. A. & Peng, X. G. Formation of high-quality CdTe, CdSe, and CdS nanocrystals using CdO as precursor. *J. Am. Chem. Soc.* **123**, 183-184 (2001).

7    Sun, S. H. & Zeng, H. Size-controlled synthesis of magnetite nanoparticles. *J. Am. Chem. Soc.* **124**, 8204-8205, doi:10.1021/ja026501x (2002).

8    Smith, A. M., Duan, H., Rhyner, M. N., Ruan, G. & Nie, S. A systematic examination of surface coatings on the optical and chemical properties of semiconductor quantum dots. *Phys. Chem. Chem. Phys.* **8**, 3895-3903, doi:10.1039/b606572b (2006).

9    Lewinski, N., Colvin, V. & Drezek, R. Cytotoxicity of nanoparticles. *Small* **4**, 26-49, doi:10.1002/smll.200700595 (2008).

10   Derfus, A. M., Chan, W. C. W. & Bhatia, S. N. Probing the cytotoxicity of semiconductor quantum dots. *Nano Lett.* **4**, 11-18 (2004).

11   Mattoussi, H. *et al.* Bioconjugation of highly luminescent colloidal CdSe-ZnS quantum dots with an engineered two-domain recombinant protein. *Physica Status Solidi B-Basic Research* **224**, 277-283 (2001).

12   Gerion, D. *et al.* Synthesis and properties of biocompatible water-soluble silica-coated CdSe/ZnS semiconductor quantum dots. *J. Phys. Chem. B* **105**, 8861-8871, doi:10.1021/jp0105488 (2001).

13   Gao, X. H., Cui, Y. Y., Levenson, R. M., Chung, L. W. K. & Nie, S. M. In vivo cancer targeting and imaging with semiconductor quantum dots. *Nat. Biotechnol.* **22**, 969-976 (2004).

14   Dubertret, B. *et al.* In vivo imaging of quantum dots encapsulated in phospholipid micelles. *Science* **298**, 1759-1762 (2002).

15   Park, J. H., von Maltzahn, G., Ruoslahti, E., Bhatia, S. N. & Sailor, M. J. Micellar hybrid nanoparticles for simultaneous magnetofluorescent imaging and drug delivery. *Angewandte Chemie International Edition-English* **47**, 7284-7288 (2008).

16   Ruan, G. *et al.* Simultaneous Magnetic Manipulation and Fluorescent Tracking of Multiple Individual Hybrid Nanostructures. *Nano Lett.* **10**, 2220-2224, doi:Doi 10.1021/Nl1011855 (2010).

17   Ruan, G. & Winter, J. O. Alternating-Color Quantum Dot Nanocomposites for Particle Tracking. *Nano Lett.* **11**, 941-945, doi:10.1021/nl103233b (2011).

18   Bae, J. *et al.* Multifunctional Nanoparticle-Loaded Spherical and Wormlike Micelles Formed by Interfacial Instabilities. *Adv. Mater.* **24**, 2735-2741, doi:10.1002/adma.201200570 (2012).

19    Xu, J. *et al.* Micelle-templated composite quantum dots for super-resolution imaging. *Nanotechnology* **25**, 195601 (2014).

20    Kim, B.-S., Qiu, J.-M., Wang, J.-P. & Taton, T. A. Magnetomicelles: Composite Nanostructures from Magnetic Nanoparticles and Cross-Linked Amphiphilic Block Copolymers. *Nano Lett.* **5**, 1987-1991, doi:10.1021/nl0513939 (2005).

21    Wang, J., Li, W. & Zhu, J. Encapsulation of inorganic nanoparticles into block copolymer micellar aggregates: Strategies and precise localization of nanoparticles. *Polymer* **55**, 1079-1096, doi:http://dx.doi.org/10.1016/j.polymer.2014.01.027 (2014).

22    Zhang, L. F. & Eisenberg, A. Multiple morphologies and characteristics of ''crew-cut'' micelle-like aggregates of polystyrene-b-poly(acrylic acid) diblock copolymers in aqueous solutions. *J. Am. Chem. Soc.* **118**, 3168-3181, doi:10.1021/ja953709s (1996).

23    Firestone, M. A., Hayden, S. C. & Huber, D. L. Greater than the sum: Synergy and emergent properties in nanoparticle-polymer composites. *Mrs Bulletin* **40**, 760-767, doi:10.1557/mrs.2015.202 (2015).

24    Bae, J. *et al.* Multifunctional Nanoparticle-Loaded Spherical and Wormlike Micelles Formed by Interfacial Instabilities. *Adv. Mater.* **24**, 2735-2741, doi:10.1002/adma.201200570 (2012).

25    Zhu, J. & Hayward, R. C. Spontaneous generation of amphiphilic block copolymer micelles with multiple morphologies through interfacial instabilities. *J. Am. Chem. Soc.* **130**, 7496-7502, doi:10.1021/ja801268e (2008).

26    Su, M. & Su, Z. Effects of Solvent Evaporation Rate and Poly(acrylic acid) on Formation of Poly(ethylene oxide)-block-polystyrene Micelles from Emulsion. *Macromolecules* **47**, 1428-1432, doi:10.1021/ma402540w (2014).

27    Nie, X., Cui, J. & Jiang, W. Ultralong cylindrical micelles precisely located with semiconductor nanorods by solvent evaporation-driven self-assembly. *Soft Matter* **10**, 8051-8059, doi:10.1039/c4sm01353k (2014).

28    Zhu, J. & Hayward, R. C. Hierarchically structured microparticles formed by interfacial instabilities of emulsion droplets containing amphiphilic block copolymers. *Angewandte Chemie-International Edition* **47**, 2113-2116, doi:10.1002/anie.200704863 (2008).

29    Nie, X. B., Cui, J. & Jiang, W. Ultralong cylindrical micelles precisely located with semiconductor nanorods by solvent evaporation-driven self-assembly. *Soft Matter* **10**, 8051-8059, doi:10.1039/c4sm01353k (2014).

30    Li, W. K. *et al.* Encapsulation of pristine fullerene C-60 within block copolymer micelles through interfacial instabilities of emulsion droplets. *J. Colloid Interface Sci.* **418**, 81-86, doi:10.1016/j.jcis.2013.12.004 (2014).

31    Geng, Y. & Discher, D. E. Hydrolytic degradation of poly(ethylene oxide)-block-polycaprolactone worm micelles. *J. Am. Chem. Soc.* **127**, 12780-12781, doi:10.1021/ja053902e (2005).

32    Duong, A. D., Ruan, G., Mahajan, K., Winter, J. O. & Wyslouzil, B. E. Scalable, Semicontinuous Production of Micelles Encapsulating Nanoparticles via Electrospray. *Langmuir* **30**, 3939-3948, doi:10.1021/la404679r (2014).

33    Sun, Y. *et al.* Examining the Roles of Emulsion Droplet Size and Surfactant in the Interfacial Instability-Based Fabrication Process of Micellar Nanocrystals. *Nanoscale Research Letters* **12**, 434, doi:10.1186/s11671-017-2202-x (2017).

34    Ding, X. Y., Han, N., Wang, J., Sun, Y. X. & Ruan, G. Effects of organic solvents on the structures of micellar nanocrystals. *RSC Advances* **7**, 16131-16138, doi:10.1039/c6ra28741g (2017).

35    Sugiyama, T. *et al.* in *Molecular Imaging for Integrated Medical Therapy and Drug Development*  (eds N. Tamaki & Y. Kuge) 139-144 (Springer, 2010).

36    Barteneva, N. & Vorobjev, I. The development of multicolor panels with Quantum Dots-conjugated antibodies for diagnostics of Chronic Lymphoid Leukemia (CLL) by conventional flow cytometer. *Nanotech Conference & Expo 2009, Vol 2, Technical Proceedings*, 26-28 (2009).

37    Wegner, K. D. *et al.* Influence of Luminescence Quantum Yield, Surface Coating, and Functionalization of Quantum Dots on the Sensitivity of Time-Resolved FRET Bioassays. *ACS Appl. Mater. Interfaces* **5**, 2881-2892, doi:10.1021/am3030728 (2013).

38    Gupta, A. K., Naregalkar, R. R., Vaidya, V. D. & Gupta, M. Recent advances on surface engineering of magnetic iron oxide nanoparticles and their biomedical applications. *Nanomed.* **2**, 23-39 (2007).

39    McBain, S. C. *et al.* Magnetic nanoparticles as gene delivery agents: enhanced transfection in the presence of oscillating magnet arrays. *Nanotechnology* **19**, - (2008).

40    Magnani, M., Galluzzi, L. & Bruce, I. J. The use of magnetic nanoparticles in the development of new molecular detection systems. *J. Nanosci. Nanotechnol.* **6**, 2302-2311 (2006).

41    Park, M. J., Park, J., Hyeon, T. & Char, K. Effect of interacting nanoparticles on the ordered morphology of block copolymer/nanoparticle mixtures. *J. Polym. Sci. Pt. B-Polym. Phys.* **44**, 3571-3579, doi:10.1002/polb.21011 (2006).

42    Zhu, J. & Hayward, R. C. Interfacial tension of evaporating emulsion droplets containing amphiphilic block copolymers: Effects of solvent and polymer composition. *J. Colloid Interface Sci.* **365**, 275-279, doi:10.1016/j.jcis.2011.09.020 (2012).

43    Schneider, C. A., Rasband, W. S. & Eliceiri, K. W. NIH Image to ImageJ: 25 years of image analysis. *Nat. Meth.* **9**, 671-675, doi:10.1038/nmeth.2089 (2012).

44    Seifert, S., Winans, R. E., Tiede, D. M. & Thiyagarajan, P. Design and performance of a ASAXS instrument at the Advanced Photon Source. *J. Appl. Crystallogr.* **33**, 782-784, doi:10.1107/s0021889800001333 (2000).

45    [http://www.sasview.org/](http://www.sasview.org/).

46    Jada, A., Hurtrez, G., Siffert, B. & Riess, G. Structure of polystyrene-block-poly(ethylene oxide) diblock copolymer micelles in water. *Macromol. Chem. Phys.* **197**, 3697-3710, doi:10.1002/macp.1996.021971117 (1996).

47    Souva, M. S., Nabar, G. M., Winter, J. O. & Wyslouzil, B. E. Vol. 512   411-418 (Journal of colloid and interface science, 2018).

48    Mortensen, K., Brown, W., Almdal, K., Alami, E. & Jada, A. Structure of PS-PEO diblock copolymers in solution and the bulk state probed using dynamic light-scattering and small-angle neutron-scattering and dynamic mechanical measurements. *Langmuir* **13**, 3635-3645, doi:10.1021/la9609635 (1997).

49    Zhang, M. *et al.* Sphere-to-Wormlike Network Transition of Block Copolymer Micelles Containing CdSe Quantum Dots in the Corona. *Macromolecules* **43**, 5066-5074, doi:10.1021/ma1004106 (2010).

50    Hickey, R. J., Haynes, A. S., Kikkawa, J. M. & Park, S.-J. Controlling the Self-Assembly Structure of Magnetic Nanoparticles and Amphiphilic Block-Copolymers: From Micelles to Vesicles. *J. Am. Chem. Soc.* **133**, 1517-1525, doi:10.1021/ja1090113 (2011).

51    Hickey, R. J. *et al.* Morphological Transitions of Block-Copolymer Bilayers via Nanoparticle Clustering. *Small* **6**, 48-51, doi:10.1002/smll.200901266 (2010).

52    Wyman, I., Njikang, G. & Liu, G. When emulsification meets self-assembly: The role of emulsification in directing block copolymer assembly. *Prog. Polym. Sci.* **36**, 1152-1183, doi:10.1016/j.progpolymsci.2011.04.005 (2011).

53    Mai, Y. & Eisenberg, A. Self-assembly of block copolymers. *Chem. Soc. Rev.* **41**, 5969-5985, doi:10.1039/c2cs35115c (2012).

54    Hotze, E. M., Phenrat, T. & Lowry, G. V. Nanoparticle Aggregation: Challenges to Understanding Transport and Reactivity in the Environment. *J. Environ. Qual.* **39**, 1909-1924, doi:10.2134/jeq2009.0462 (2010).

55    Burke, S. E. & Eisenberg, A. Kinetics and mechanisms of the sphere-to-rod and rod-to-sphere transitions in the ternary system PS310-b-PAA(52)/dioxane/water. *Langmuir* **17**, 6705-6714, doi:10.1021/la010640v (2001).

56    Bockstaller, M., Kohler, W., Wegner, G., Vlassopoulos, D. & Fytas, G. Levels of structure formation in aqueous solutions of anisotropic association colloids consisting of rodlike polyelectrolytes. *Macromolecules* **34**, 6359-6366, doi:10.1021/ma010027i (2001).

57    Mang, J. X., Li, S. H., Li, X. D., Li, X. H. & Zhu, K. J. Morphology modulation of polymeric assemblies by guest drug molecules: TEM study and compatibility evaluation. *Polymer* **50**, 1778-1789, doi:10.1016/j.polymer.2009.02.004 (2009).

58    Van Krevelen, D. W. in *Properties of Polymers: Their Correlation with Chemical Structure; Their Numerical Estimation and Prediction from Additive Group Contributions* 189-227 (Elsevier, Amsterdam, The Netherlands, 2009).

59    Born, P. & Kraus, T. Ligand-dominated temperature dependence of agglomeration kinetics and morphology in alkyl-thiol-coated gold nanoparticles. *Physical Review E* **87**, doi:10.1103/PhysRevE.87.062313 (2013).

60    Sperling, R. A. & Parak, W. J. Surface modification, functionalization and bioconjugation of colloidal inorganic

nanoparticles. *Philos. Trans. R. Soc. A-Math. Phys. Eng. Sci.* **368**, 1333-1383, doi:10.1098/rsta.2009.0273 (2010).

61      Damasceno, P. F., Engel, M. & Glotzer, S. C. Predictive Self-Assembly of Polyhedra into Complex Structures. *Science* **337**, 453-457, doi:10.1126/science.1220869 (2012).

62      van Sark, W. G. J. H. M. *et al.* Photooxidation and Photobleaching of Single CdSe/ZnS Quantum Dots Probed by Room-Temperature Time-Resolved Spectroscopy. *The Journal of Physical Chemistry B* **105**, 8281-8284, doi:10.1021/jp012018h (2001).

63      Zrazhevskiy, P., Sena, M. & Gao, X. H. Designing multifunctional quantum dots for bioimaging, detection, and drug delivery. *Chem. Soc. Rev.* **39**, 4326-4354, doi:10.1039/b915139g (2010).

64      Xu, J. *et al.* Simultaneous, single particle, magnetization and size measurements of micron sized, magnetic particles. *J. Magn. Magn. Mater.* **324**, 4189-4199 (2012).
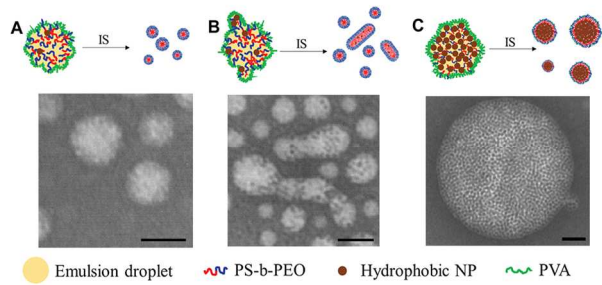
Nanoparticle loading changes both internal and overall micelle structure.